THE JOURNAL OF PHYSICAL CHEMISTRY C
A JOURNAL OF THE AMERICAN CHEMICAL SOCIETY

pubs.acs.org/JPCC

Article

Ultrafast Optical Spin Switching in Ferrimagnetic Nickel Ferrite ($NiFe_2O_4$) Studied by XUV Reflection–Absorption Spectroscopy

Stephen Londo, Somnath Biswas, Igor V. Pinchuk, Alexandra Boyadzhiev, Roland K. Kawakami, and L. Robert Baker*

Cite This: *J. Phys. Chem. C* 2022, 126, 2669–2678

Read Online

ACCESS | Metrics & More | Article Recommendations | Supporting Information

ABSTRACT: The ability to optically manipulate spin states has potential to enable ultrafast magnetization switching at rates that are several orders faster than magnetic precession. However, controlling these processes requires understanding of the site-specific charge transfer and spin dynamics during optical excitation and subsequent hot carrier relaxation. Nickel ferrite (NFO) is a ferrimagnetic semiconductor with potential for ultrafast switching. Because of the partial degree of inversion, 12 possible charge transfer excitations exist in NFO. Using extreme ultraviolet reflection–absorption (XUV-RA) spectroscopy to measure the Fe M-edge, Ni M-edge, and O L-edge spectra with femtosecond time resolution reveals that 400 nm light excites an electron transfer from O 2p valence band states to Fe 3d conduction band states. Kinetic analysis shows that this charge transfer state undergoes fast electron and hole polaron formation, where electrons localize to O_h Fe centers and holes localize to O_h Ni centers. Hole polaron formation increases the crystal field splitting around Ni which drives a spin-state transition leading to a low-spin O_h Ni^{3+} final state within 0.326 ± 0.14 ps. This study reveals the mechanism of ultrafast optical spin switching in NFO and highlights the capability of XUV spectroscopy to elucidate these dynamics with unprecedented temporal and site-specific resolution.

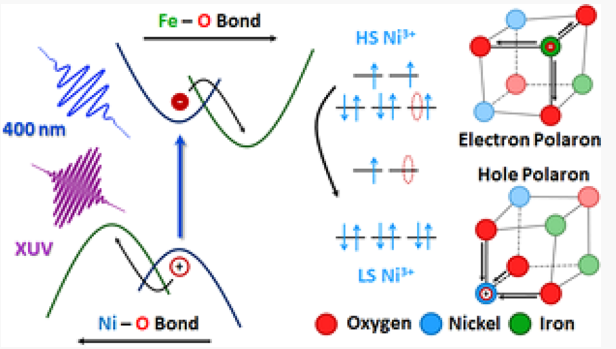

INTRODUCTION

As modern electronic devices gradually increase their operation speed and storage requirements, there has been a push to find faster methods to process this stored information. Magnetic memory devices address this concern by storing information within magnetic domain in either "up" or "down" spin states, representing the standard logical bits of "ones" and "zeroes". Unfortunately, magnetic precession governs the time scale of switching between these magnetic states, limiting the operational speeds to no faster than several picoseconds.[1] This limitation can be overcome, however, through the application of femtosecond laser pulses, which has demonstrated subpicosecond control over the magnetization of a material.[2−5] This control has been observed in several types of ferrimagnetic alloys containing Gd, Tb, Dy, and Ho[6−8] for use in fast, energy-efficient memory devices as well as ferromagnetic stacks of Pt and Co.[9,10] Additionally, optical control of a material's magnetization control has been further extended to include semiconductor materials,[11−13] including magnetic metal oxides.[14,15]

One theory attempting to explain the mechanism of this control is that changes in the magnetocrystalline anisotropy are caused by optically induced electron transfer between nonequivalent sites within the crystal structure.[16−19] This change in anisotropy enables control of magnetization on a subpicosecond time scale because electron transfer and resulting electron–phonon coupling are not limited by the frequency of magnetic precession. Electron–phonon coupling changes the nuclear positions and modulates magnetocrystalline anisotropy on the femtosecond time scale.

Ultrafast demagnetization and spin switching have been extensively studied in metals.[20−22] These studies show that optically induced demagnetization in metals occurs via spin heating from electron–electron scattering (<0.1 ps), which is significantly faster than electron–phonon scattering (>1 ps).[23,24] However, in magnetic oxides the mechanism may be quite different. In semiconducting or insulating oxides, electron–electron scattering is slower due to their much lower electron density compared to metals.[25] Additionally, charge transfer in a polar oxide lattice results in strong electron–phonon coupling and small polaron formation on the subpicosecond time scale.[26−28] Small polarons significantly modify the crystal field splitting and magnetocrystalline

Received: November 12, 2021
Revised: January 24, 2022
Published: February 2, 2022

https://doi.org/10.1021/acs.jpcc.1c09763
J. Phys. Chem. C 2022, 126, 2669–2678

anisotropy. Consequently, mechanistic understanding of optically induced spin transitions in magnetic oxides requires the ability to measure charge transfer and electron−phonon scattering with site specific resolution on the femtosecond time scale, something that has traditionally been quite challenging.

The complexity of this challenge is illustrated for the ferrimagnetic semiconductor, nickel ferrite (NFO). NFO is a metal-oxide semiconductor belonging to the class of spinel ferrites and has been used in various spin-based device applications.[29,30] It has the chemical formula $[Ni_{1-x}^{2+}Fe_x^{3+}]_{T_d}[Ni_x^{2+}Fe_{2-x}^{3+}]_{O_h}O_4$, where x represents the degree of inversion and its crystal structure is shown in Figure 1a. NFO thermodynamically assumes an *inverse* spinel

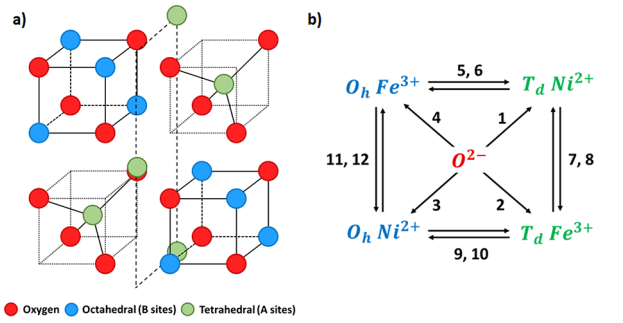

Figure 1. (a) Spinel crystal structure of NFO. O sites are red, O_h metal sites are blue, and T_d metal sites are green. Note that both O_h and T_d sites can be occupied by either Fe^{3+} or Ni^{2+} because of the partial inversion of NFO. (b) Twelve possible excitation pathways are available to the mixed spinel structure of NFO: LMCT from O to T_d (1,2) and O_h (3,4) metal sites, MMCT to and from O_h and T_d sites (5,6 and 9,10), and MMCT between two T_d (7,8) or two O_h (11,12) sites.

structure (x = 1) indicating that Ni^{2+} ions populate half of the octahedral (O_h) sites and Fe^{3+} ions populate the remaining half of the O_h sites and all of the tetrahedral (T_d) ones. However, in practice, the degree of inversion may be less than unity. For example, NFO samples studied here have a degree of inversion of x = 0.73 as determined by X-ray photoelectron spectroscopy (see the Supporting Information, section 2).

Because of the incomplete inversion, a portion of the Ni^{2+} ions occupy T_d lattice sites. Considering the photophysics of this complex oxide, there are 12 possible optically induced electronic transitions that could occur upon photoexcitation: four ligand-to-metal charge-transfer (LMCT) pathways from O 2p to the four metal cations and eight metal-to-metal charge-transfer (MMCT) transitions between the different metal cations at both O_h and T_d sites. These 12 transitions are depicted schematically in Figure 1b with arrows indicating the direction of electron transfer between various lattice sites. Additionally, in the ground state of NFO both metal centers (Fe^{3+} and Ni^{2+}) are in the high-spin state with the O_h and T_d sublattices aligned antiparallel to each other.[31] To discern between these charge transfer excitations and observe the effect on magnetocrystalline anisotropy on the ultrafast time scale with site-specific resolution is a challenging but important goal toward the rational design of optically switchable magnetic materials.

One method to differentiate between these possible charge transfer excitations is through X-ray absorption spectroscopy (XAS), an element specific technique with the ability to probe the oxidation state, spin configuration, and crystal field geometry of each metal center in a complex material.[32] Traditionally, XAS is limited to ∼100 ps time resolution due to the pulse duration of X-ray light produced at third-generation synchrotrons, making this method too slow for studies of ultrafast optical switching. However, extreme ultraviolet (XUV) spectroscopy based on laser-driven high-harmonic generation (HHG) combines the element, oxidation, and spin-state resolution of XAS with ultrafast time resolution.[33−36] HHG relies on the nonlinear upconversion of femtosecond laser light to produce a broadband XUV pulse spanning 10s to 100s of eV in photon energy. This tabletop method is ideal for measuring the M-edges of the 3d transition metals with femtosecond, or even attosecond, time resolution.[26,37−39] Additionally, there have been several studies of t-MOKE which benefit from the incorporation of XUV light to probe the magnetization dynamics of materials.[40−42] Our group has

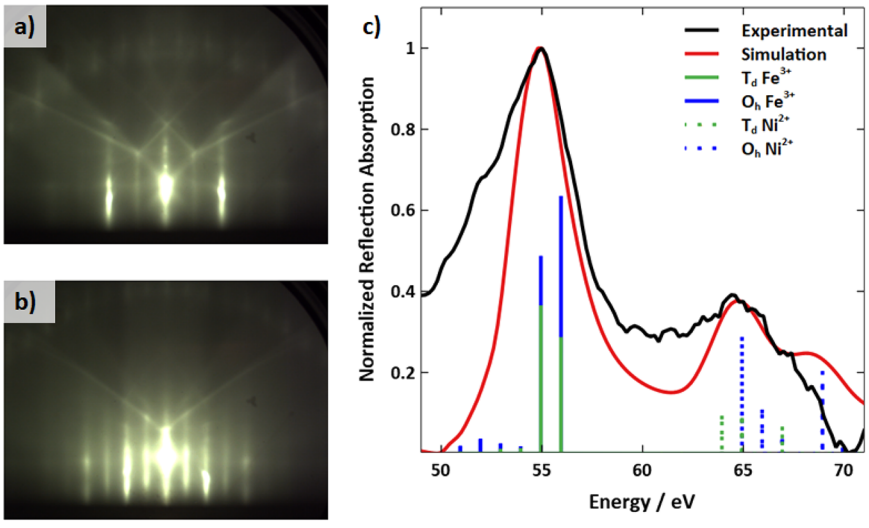

Figure 2. (a) and (b) RHEED measurements demonstrating the high-quality nature of the 40 nm thick, NFO thin films. (c) Experimental ground-state spectrum of NFO overlaid with a simulated spectrum using our semiempirical method. The stick spectra for the four atomic centers that comprise the final simulated spectrum (red) are shown as solid (Fe^{3+}) or dashed (Ni^{2+}) lines.

https://doi.org/10.1021/acs.jpcc.1c09763
J. Phys. Chem. C 2022, 126, 2669−2678

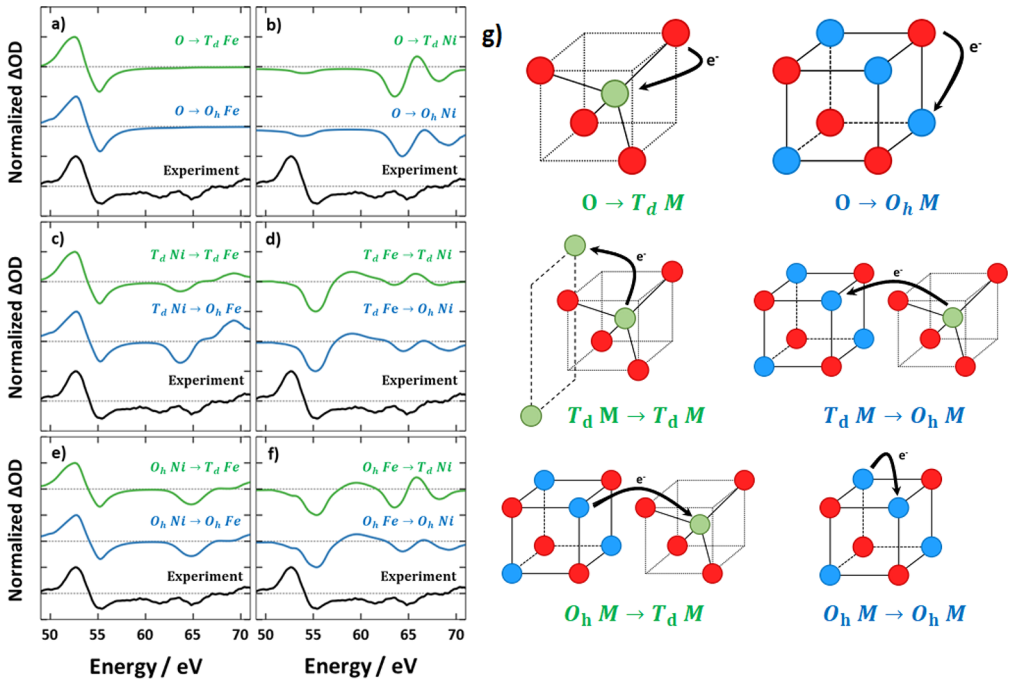

Figure 3. Experimental transient XUV spectrum (black) compared to the 12 excitation pathways available in the mixed spinel phase: (a) LMCT from O to Fe, (b) LMCT from O to Ni, (c) MMCT from T_d Ni to Fe, (d) MMCT from T_d Fe to Ni, (e) MMCT from O_h Ni to Fe, and (f) MMCT from O_h Fe to Ni. (g) Schematic illustrating the electron transfer process associate with each of the simulated transitions.

recently developed a reflection−absorption analogue of XUV transient absorption that enables studies of highly crystalline epitaxial films without limitations on sample thickness or substrate.[43] Here we utilize XUV reflection−absorption spectroscopy to probe the site-specific dynamics in photo-excited NFO. These results provide a clear mechanistic picture of the photoinduced charge transfer excitation leading to an ultrafast spin transition from Ni^{2+} high spin to Ni^{3+} low spin within ∼0.3 ps following photoexcitation.

METHODS

NFO films are grown on magnesium oxide (MgO) substrates by molecular beam epitaxy (MBE) through co-evaporation of Ni and Fe under a molecular oxygen partial pressure of $\sim 5 \times 10^{-7}$ Torr. Details of the growth are provided in the Supporting Information (section 1). As shown in Figures 2a and 2b, the reflection high-energy electron diffraction (RHEED) from a 40 nm NFO film on MgO(001) exhibits a streaky pattern, which is indicative of two-dimensional layer-by-layer growth with single crystalline order. The distinct patterns for the RHEED beam along the [100] (Figure 2a) and [110] in-plane directions (Figure 2b) arise from the cube-on-cube epitaxial relationship between the NFO film and MgO substrate.

For the purposes of this study, we have performed XUV reflection−absorption spectroscopy to simultaneously probe the Fe and Ni $M_{2,3}$-edge absorption edges for both static and time-resolved measurements. XUV light is produced by using tabletop high-harmonic generation with a two-color driving field focused into a He-filled semifinite gas cell. This two-color driving field breaks the inversion symmetry of the electric field, enabling the generation of both even and odd harmonics, effectively producing a white-light source over a 36−72 eV probing range. The XUV light is focused onto the NFO samples at 82° relative to the surface normal and optically excited by using a 400 nm pump beam. The reflected XUV light is spectrally separated and detected with a CCD camera. Additional details of the experimental setup are provided in the Supporting Information (section 3).

Taking the degree of inversion calculated by XPS, it is possible to predict the XUV reflection−absorption spectrum at the Fe and Ni $M_{2,3}$-edges starting from a ligand-field multiplet simulation performed by using CTM4XAS.[44] This simulation predicts the atomic multiplet structure of the metal cations in ground (Fe^{3+} and Ni^{2+}) and exited ($Fe^{2+/4+}$ and $Ni^{1+/3+}$) oxidation states for both O_h and T_d coordination environments. The resulting sticks spectra representing contributions from O_h (blue) and T_d (green) centers are shown in Figure 2c, with solid lines showing the Fe $M_{2,3}$-edge spectrum and dashed lines showing the Ni $M_{2,3}$-edge spectrum. Following calculations of the sticks spectra using CTM4XAS, the reflection−absorption spectrum is obtained by first broadening these sticks by using a Lorentz−Fano profile followed by Kramers−Kronig transformation to convert the absorption spectrum to a complex refractive index. Finally, the reflection−absorption spectrum is obtained by the p-polarized Fresnel equation accounting for surface roughness by using the Debye−Waller factor as described previously.[38] Additional details are provided in the Supporting Information (section 4). The resulting predicted XUV reflection−absorption spectrum is shown in Figure 2c (red) and provides a qualitatively good match to the measured experimental ground state (black). From this we see that the XUV spectrum provides signatures for each of the four metal centers present in this system: O_h Fe^{3+}, T_d Fe^{3+}, O_h Ni^{2+}, and T_d Ni^{2+}. Below we show that the transient XUV spectrum is also able to resolve between the 12 different charge-transfer excitations possible in this material, providing a chemically precise assignment for the photoexcited state of NFO.

https://doi.org/10.1021/acs.jpcc.1c09763
J. Phys. Chem. C 2022, 126, 2669−2678

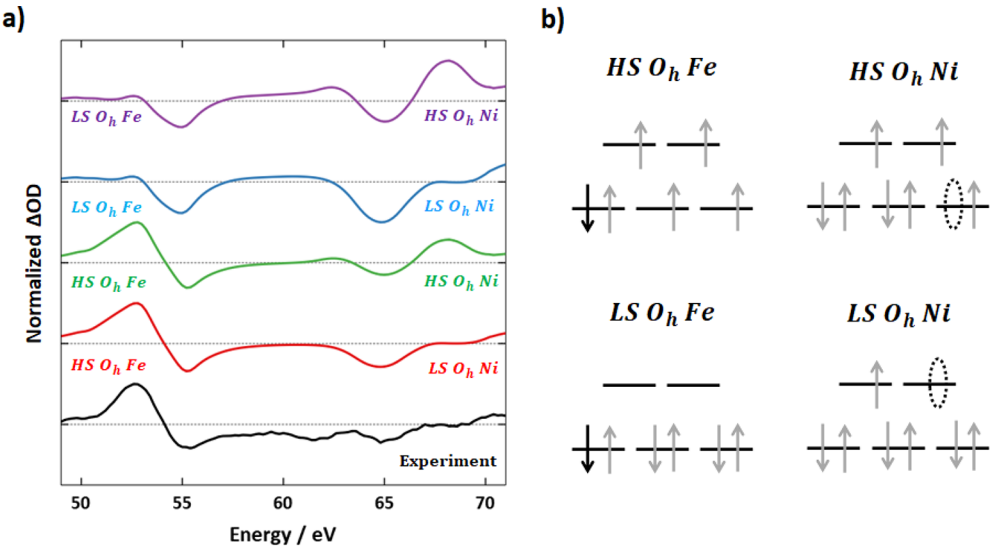

Figure 4. (a) Experimental transient XUV spectrum (black) compared to the four possible excited-state spin configurations following a MMCT transition from O_h Ni to O_h Fe: LS Ni and HS Fe (red), HS Ni and HS Fe (green), LS Ni and LS Fe (blue), HS Ni and LS Fe (purple). (b) Orbital diagrams of the possible electron spin configurations for HS/LS Fe^{2+} and Ni^{3+} included in each of the simulations.

RESULTS AND DISCUSSION

With this groundwork in place, we can now simulate transient XUV spectra for each of the 12 excitation pathways depicted in Figure 1b and compare them against experimental observations. Transient spectra were measured at 20 time delays between 0 and 5 ps. We find that while significant spectral evolution occurs during the first 0.2 ps following photoexcitation, the transient spectrum remains nearly constant for time delays greater than 0.3 ps. Here we first assign the final transient spectrum, which represents the equilibrated excited state, taken as an average of all measured time delays greater than 0.3 ps. Following the assignment of the site specific oxidation and spin states from this spectrum, we then describe the ultrafast time evolution of the spectrum to provide a clear picture of the mechanism for ultrafast optical spin-state switching in NFO. This experimental transient spectrum is shown in black in Figures 3a–f for comparison to simulated spectra of 12 possible charge transfer transitions in NFO. Simulations of the various possible excitation pathways have been grouped for clarity. LMCT transitions (O 2p → M 3d) are shown in Figures 3a and 3b, MMCT transitions with the donated electron originating at tetrahedral metal sites (T_d M 3p → M 3d) are Figures 3c and 3d, and MMCT transitions with the donated electron originating at octahedral metal sites (O_h M 3p → M 3d) are depicted in Figures 3e and 3f. Additionally, the left column (3a, 3c, and 3e) shows photoexcited electrons localizing to Fe^{3+} reducing the metal center to Fe^{2+} and oxidizing the ligand or Ni^{2+} centers to either O^{1-} or Ni^{3+}, respectively. The right column (3b, 3d, and 3f) shows photoexcited electrons localizing to Ni^{2+} reducing it to Ni^{1+} and oxidizing either the ligand or Fe^{3+} to O^{1-} or Fe^{4+}, respectively. Finally, diagrams depicting the charge-transfer transitions associated with each of the simulated transient spectrum are displayed to the right of the spectra (Figure 3g). In this schematic, blue spheres represent O_h metal centers, green spheres represent T_d metal centers, and red spheres represent O^{2-} anions. Note that O_h and T_d metal centers can be either Fe^{3+} or Ni^{2+} because of the partial inversion.

The same experimental transient spectrum is shown in each panel in black for comparison with the various simulated transients. Starting with the LMCT transitions (Figures 3a and 3b), it can clearly be seen that these do not agree well with experimental findings because the experimental spectrum displays features at both the Fe- and Ni-edges. This implies that the spectral signature at time delays greater than 0.3 ps resembles a MMCT transition state, and this is consistent with previous experiments on CFO.[45] Additionally, reduction of Fe^{3+} is predicted to result in an excited-state absorption peak at 53 eV and a ground-state bleach at 55 eV[27] which can be seen in Figure 3a. This agrees well with the experimental spectra. However, the reduction of Ni^{2+} depicted in Figure 3b is predicted to result in two ground-state bleaches at 63 and 68 eV and an excited-state absorption at 66 eV,[46] which are not observed in the experimental spectra. This indicates that electron transfer occurs from a Ni^{2+} site to an Fe^{3+} upon 400 nm optical excitation of NFO, and this conclusion allows us to eliminate the other four excited states from the right column (Figures 3d and 3f). The remaining four possible transitions are an electron transfer from T_d Ni or O_h Ni sites to either T_d Fe or O_h Fe centers depicted in Figures 3c and 3e, respectively. Of these possible MMCT transitions, excitation from T_d Ni centers represent a poor fit to the experiment as both the simulated bleach and excited-state absorption features resulting from oxidation of Ni^{2+} are ∼1 eV red-shifted from those seen in the experimental spectrum at 65 and 70 eV. The last two transitions agree well with experimental results in the relative intensity of observed spectral features as well as having the proper energy positions for the excited-state absorption and bleach features at both the Fe- and Ni-edges. There is a subtle difference between the O_h Ni → O_h Fe and O_h Ni → T_d Fe spectra in that a small shoulder is present at 51 eV for O_h Fe which is seen in the experimental spectrum. Additionally, the through-space coupling distance for an O_h → O_h transition in the spinel structure is significantly shorter (∼2.8 Å) than an O_h → T_d transition (∼3.3 Å). From this we hypothesize that photoexcitation of NFO primarily results in a MMCT transition whereby electrons from O_h Ni sites transfer to O_h Fe sites, reducing Fe and oxidizing Ni metal centers.

https://doi.org/10.1021/acs.jpcc.1c09763
J. Phys. Chem. C 2022, 126, 2669−2678

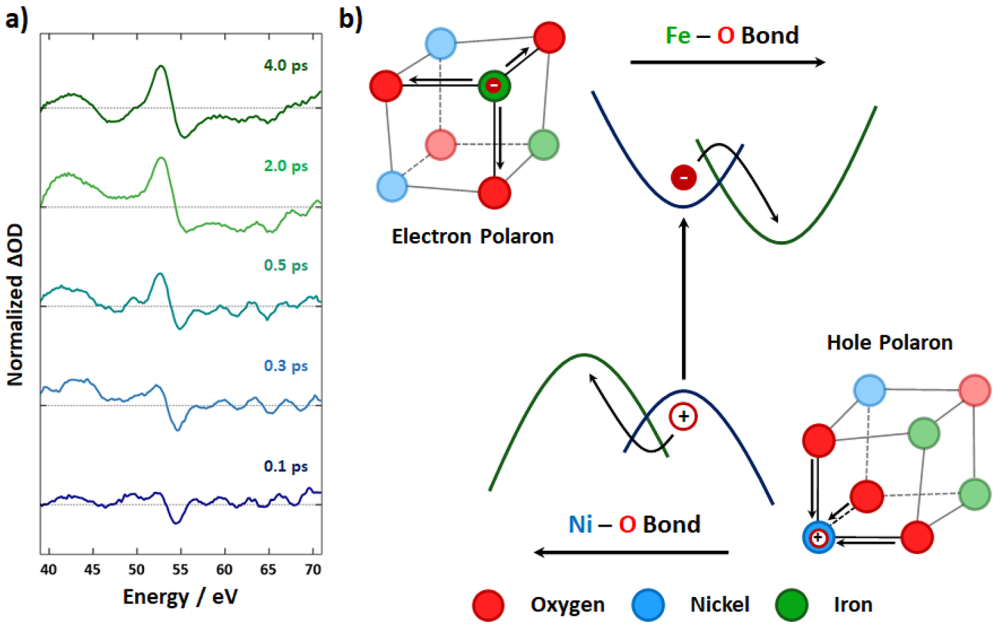

Figure 5. (a) Transient time-averaged XUV spectra representing select time delays and depicting the evolution of the O L-edge (40−50 eV), Fe M-edge (50−60 eV), and Ni M-edge (60−70 eV). (b) Cartoon representation of the electron and hole free carrier (blue) and polaron (green) states involved after photoexcitation. Distortion of the lattice due to localized carriers causes polaron formation around excited Fe (lattice expansion) and Ni (lattice compression) O_h sites.

Above we have assigned the element-specific oxidation-state changes associated with the photoinduced charge transfer excitation of NFO. We now consider the possibility that this charge transfer transition induces a spin transition at either the Fe or Ni centers. The MMCT excitation results in a Fe^{2+}/Ni^{3+} final state, which can exist in four possible spin configurations: LS Ni^{3+}/ HS Fe^{2+}, HS Ni^{3+}/ HS Fe^{2+}, LS Ni^{3+}/ LS Fe^{2+}, and HS Ni^{3+}/ LS Fe^{2+}. Simulated transient spectra of these possible spin states are shown in Figure 4a for comparison to the experimental transient spectrum. Also shown are the excited-state electron configurations for HS/LS Fe^{2+} and Ni^{3+} associated with these spin-state configurations (Figure 4b).

The simulated spectra representing LS Fe (Figure 4a, blue and purple) represent a poor fit to the experiment possessing only a bleach in the Fe M-edge at 55 eV and no excited-state absorption feature as is present in the experimental spectrum at 53 eV. This allows us to eliminate LS Fe^{2+} from the possible spin configurations. Considering the Ni M-edge region, while both of these spectra show a ground-state bleach at 65 eV, the excited-state absorption seen in the HS Ni → HS Fe simulation (green) at 68 eV is red-shifted from the observed feature in the experimental spectrum but is properly captured in the LS Ni → HS Fe simulation (red). It is important to note that the observed formation of LS O_h Ni^{3+} cannot be obtained through a MMCT due to the ferromagnetic alignment between the Fe and Ni O_h sites in NFO. From this analysis, we hypothesize that photoexcited NFO thin films localize to a LS O_h Ni → HS O_h Fe MMCT state and undergo a spin-state transition from native Ni HS to LS on the ultrafast time scale.

Considering the mechanism for ultrafast spin relaxation, following optical excitation hot carriers relax rapidly via carrier−phonon scattering. This serves to decrease the population of electrons and holes due to fast equilibration with optical phonons. The time constant for optical phonon scattering in metal oxides has been reported to be faster than 40 fs.[26,47] Following the creation of a hot phonon population, these optical phonons couple to free carriers to produce self-trapped charges in the form of small polarons. Reported time constants for polaron formation are in the order of several hundred femtoseconds.[26,27,47] Polarons can be classified as large or small, depending on the extent of carrier localization with respect to the size of the unit cell. Recent XUV measurements have shown that in the transition metal oxides Fe_2O_3, Co_3O_4, and NiO free carriers form small polarons with a radius on the order of a single M−O bond length, indicating near single site localization in these materials.[48]

Small polarons can stabilize both electron and holes. While electron polarons are commonly observed in transition metal oxides, hole polarons tend to form when the positive charge is localized to metal 3d states having a lower dispersion compared to O 2p valence band states.[49,50] In NFO, the valence band maximum consists primarily of filled Ni 3d states.[51] While initial optical excitation with 400 nm light has sufficient energy to promote an electron from the lower lying O 2p valence band states to the conduction band, carrier−phonon scattering will result in hole thermalization to Ni 3d states at the valence band maximum, indicating that both electron and hole polaron formation are expected in NFO.

To address the mechanism of spin crossover, we consider the change in local crystal field splitting induced by polaron formation. Electron polaron formation results from reduction of Fe^{3+} to Fe^{2+}, leading to reduced electrostatic attraction between the Fe center and its negatively charge O ligands. This creates a lattice distortion that can be characterized as an expansion of the Fe−O bond and leads to decreased crystal field splitting. This decrease in the crystal field splitting would stabilize the already high-spin nature of Fe in the excited state, consistent with experimental observation (Figure 4). In contrast, hole polaron formation results from oxidation of Ni^{2+} to Ni^{3+}. By similar logic, this would result in contraction of the Ni−O bond length and an increase in the excited-state crystal field splitting. This increased crystal field splitting could

https://doi.org/10.1021/acs.jpcc.1c09763
J. Phys. Chem. C 2022, 126, 2669−2678

Figure 6. Pictorial representation of the rate processes in polaron formation whereby photoexcitation from the ground state produces free electrons and holes that generate optical phonons (1). These then couple to free electrons (2) and hole (3) to form electron and hole polarons, respectively.

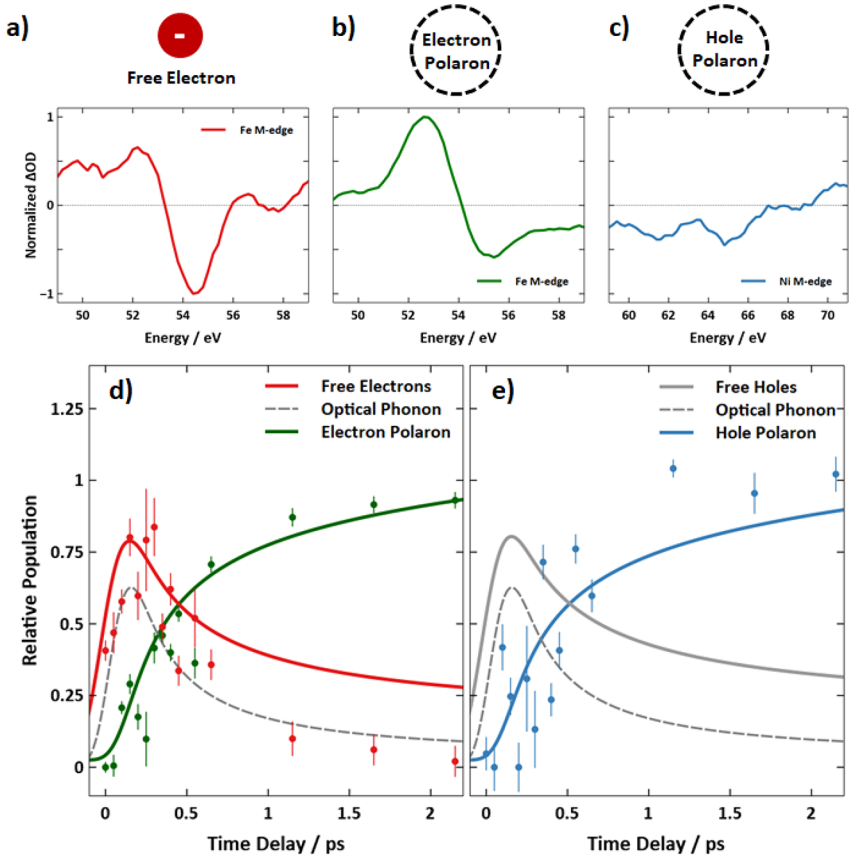

Figure 7. Experimental XUV traces corresponding to the different states in electron and hole polaron formation, namely the (a) free electron, (b) electron polaron, and (c) hole polaron states. The free hole state would likely be derived from the O L-edge signature but is convoluted with hole polaron formation and is therefore excluded. Amplitude coefficients of these states are then fit to a modified version of the two-temperature model to determine the rates of (d) electron and (e) hole polaron formation.

represent a driving force for spin crossover, leading to low-spin Ni^{3+} centers and would be consistent experimental observations.

Figure 5a shows the time evolution of the experimental transient spectra measured at 0.1, 0.3, 0.5, 2.0, and 4.0 ps time delays. As described above, the region from 50 to 60 eV represents the Fe M-edge, and the region between 60 and 70 eV represents the Ni M-edge. Also shown at lower energy (38−48 eV) is the O L-edge or the core-hole transition from O 2s to O 2p states. Note that no O L-edge signal is observed in the static-state spectrum because in the ground state of NFO, O ligands have a −2 charge. This corresponds to a full $2s^2\ 2p^6$ electron configuration, which precludes a 2s → 2p transition. However, the appearance of positive absorption at the O L-edge in the transient spectra can reflect the presence of a hole in the O 2p valence band as well as increased M−O bond covalency resulting from electron−phonon coupling following photoexcitation.

We have already assigned the late time delay spectra (2.0 and 4.0 ps) as a HS O_h Fe^{2+}/LS O_h Ni^{3+} photoexcited state, resulting from charge transfer and an associated spin transition leading to LS O_h Ni^{3+}. We now consider the mechanism for

https://doi.org/10.1021/acs.jpcc.1c09763
J. Phys. Chem. C 2022, 126, 2669−2678

this spin transition. As shown in Figure 5a, at the earliest time delays (0.1 and 0.3 ps), we observe transient signal only at the O L-edge and Fe M-edge. This signal indicates a LMCT excitation where an electron is promoted from the O 2p valence band to the Fe 3d conduction band of NFO. We find that the Fe M-edge spectrum changes line shape as a function of time over the first several hundred femtoseconds. This change in spectral shape at the Fe M-edge has been studied previously and is the result of electron polaron formation at photoexcited O_h Fe^{2+} centers.[27] On a similar time scale we also observe an increase in intensity at the O L-edge as well as the appearance of transient signal at the Ni M-edge, indicating formation of LS O_h Ni^{3+}. Both the O L-edge and Ni M-edge spectral evolution are consistent with formation of a hole polaron. To explain, a hole polaron involves contraction of negatively charged O ligands around photoexcited Ni^{3+}, which occurs as the hot hole thermalizes from O 2p to Ni 3d valence band states. This increases the crystal field splitting around Ni^{3+} favoring a low-spin configuration. It also increases mixing between Ni 3d and O 2p orbitals, leading to increased absorption at the O L-edge.

This process of electron and hole polaron formation at Fe^{2+} and Ni^{3+} centers, respectively, is schematically depicted in Figure 5b. From this figure, it can be seen that adjacent O_h Fe and O_h Ni centers share two O ligands. Expansion of these Fe−O bonds leads to contraction of the associated Ni−O bonds, indicating that electron and hole polaron formation in NFO may proceed along a single, concerted reaction coordinate. To evaluate this hypothesis, we performed a global fit of the transient XUV spectra to a kinetic model where photoexcitation produces a population of free electrons and holes that rapidly equilibrate with optical phonons with a rate constant of k_{op}. Following equilibration of free carriers with optical phonons, electrons couple with phonons to produce electron polarons with a time constant of $k_{pol(-)}$, and holes couple with phonons to produce hole polarons with a time constant of $k_{pol(+)}$. This model is schematically depicted in Figure 6, and the associated rate equations are provided in the Supporting Information (section 5). Note that this model does not differentiate between the formation of multiple distinct optical phonon modes or whether the carrier−phonon coupling is strongest for electrons or holes. The reason for this limitation is that, as reported below, the observed rate constant for k_{op} is faster than the instrument limited resolution of these experiments (<50 fs), so it is not possible to experimentally resolve these details in this study.

To determine time-dependent populations, each transient spectrum is fit as a linear combination of spectral vectors representing N_e (free electrons), $N_{pol(-)}$ (electron polarons), and $N_{pol(+)}$ (hole polarons). In this analysis, N_e is taken as the initial Fe M-edge spectrum at t = 0 ps, $N_{pol(-)}$ is taken as the final Fe M-edge spectrum at t > 2 ps, and $N_{pol(+)}$ is taken as the final Ni M-edge spectrum at t > 2 ps. These spectral vectors are shown in Figure 7a−c. The O L-edge is not included in this kinetic analysis because it contains contributions both from hot holes in the O 2p valence band as well as mixing of the Ni 3d and O 2p states following polaron formation. Consequently, it cannot be cleanly mapped to a single state but reflects contributions of both free holes and hole polarons. Although no observable provides unambiguous time-dependent population of free holes, we can still fit N_e, $N_{pol(-)}$, and $N_{pol(+)}$ as a function of time to determine the elementary rate constants k_{op}, $k_{pol(-)}$, and $k_{pol(+)}$. This analysis does not implicitly assume a concerted process for electron and hole polaron formation but instead treats these processes as independent. However, in the case that the rate constants for electron and hole polaron formation are identical within error, we hypothesize that electron and hole polaron formation are likely to proceed along a single, concerted reaction coordinate.

Results of this kinetic analysis are shown in Figure 7. Figure 7d shows the experimental populations and fits for electron polaron formation, while Figure 7e shows the experimental populations and fits for hole polaron formation. The associated time constants resulting from these fits are summarized in Table 1. Comparing the rates for electron and hole polaron formation, we see the time constants for electron ($\tau_{pol(-)}$ = 0.297 ± 0.10 ps) and hole ($\tau_{pol(+)}$ = 0.326 ± 0.14 ps) polaron are nearly identical. From this we conclude that electron and hole polaron formation appears to be coupled, suggesting that electron and hole polarons form along a concerted reaction coordinate due to the shared O ligands within the O_h sublattice. In these measurements, we do not observe a transient spectrum of HS Ni; instead, the appearance of signal at the Ni M-edge evolves directly into the spectrum we have previously assigned to LS O_h Ni^{3+} (see Figures 4 and 5). This indicates that the rate of intersystem crossing is at least as fast as hole polaron formation, setting 0.326 ± 0.14 ps as an upper bound on the time required for spin crossover leading to LS O_h Ni^{3+} centers in NFO.

Table 1. Measured Rates and Associated Time Constants for Optical Phonon Scattering, Electron Polaron Formation, and Hole Polaron Formation

	rate constant (ps^{-1})	time constant (ps)
optical phonon	180.8 ± 3040	0.006 ± 0.093
electron polaron	3.37 ± 1.17	0.297 ± 0.103
hole polaron	3.07 ± 1.36	0.326 ± 0.145

Unfortunately, we cannot conclude from spectral simulations alone whether a spin crossover event occurs on O_h Ni^{3+} after electron transfer from Ni 3d to O 2p states or if spin crossover occurs on O 2p states prior to electron transfer. However, the observed rate closely follows the bond length changes resulting from polaron formation, indicating that this process is driven by nuclear motion. This observation suggests that contraction of the Ni−O bond, which increases the crystal field splitting between Ni e_g and t_{2g} orbitals, represents the likely driving force for spin crossover. From this we hypothesize that a spin-state transition occurs on O_h Ni^{3+} as a result of hole polaron formation; however, we cannot exclude the possibility of spin crossover on O 2p states followed by a spin-allowed electron transfer, which would also result in the experimentally observed LS O_h Ni^{3+} final state. Additionally, it is possible that spin crossover occurs on O_h Ni^{2+}. Because a transition to a LS (S = 0) O_h Ni^{2+} state would not change the occupancy of either the e_g or t_{2g} orbitals, this intermediate would be XUV dark. While we cannot exclude this intermediate from spectral simulations alone, the kinetic analysis indicates this pathway is less probable. To explain, we observe that formation of the O_h LS Ni^{3+} final state is correlated in time with small polaron formation, suggesting that the spin-state transition is coupled to the lattice distortion. In contrast to Ni^{3+}, spin crossover on O_h Ni^{2+} experiences no occupancy change in either the e_g or t_{2g} orbitals, so formation of this ligand field excited state would be relatively decoupled

https://doi.org/10.1021/acs.jpcc.1c09763
J. Phys. Chem. C 2022, 126, 2669−2678

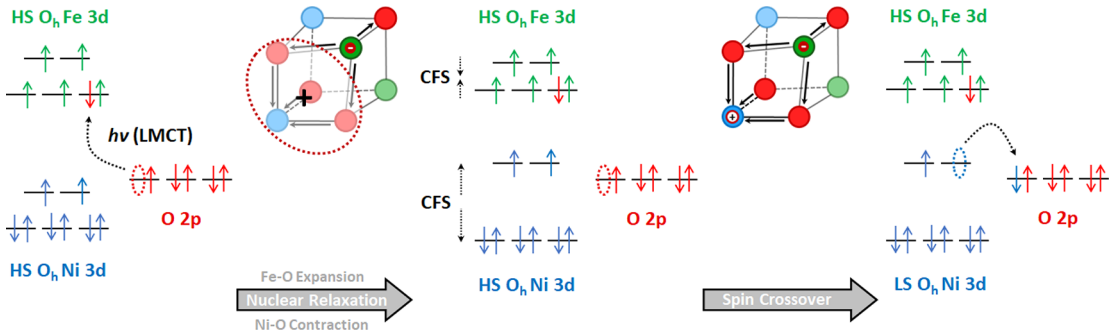

Figure 8. Schematic diagram depicting the process of spin crossover in NFO thin films. An initial LMCT state induces electron polaron formation around excited O_h Fe sites and delocalizes hole density around surrounding O ligands. The resulting lattice distortion compresses the Ni−O bonds of shared O atoms, increasing the crystal field splitting for Ni sites and decreasing it for Fe sites. Hole density then localizes to the compressed O_h Ni atom, further reducing the Ni−O bond length and forming hole polarons. The increased crystal field splitting stabilizes the LS configuration and causes excited Ni atoms to spin flip from their initial HS state.

from the nuclear motion. Consequently, while spectral simulations cannot exclude the presence of a O_h LS Ni^{2+} intermediate, we consider the pathway involving spin crossover O_h Ni^{3+} is more probable.

With this in mind, we construct a picture of what occurs in photoexcited NFO thin films and assign the evolution of the spectra to elementary processes. Initially after photoexcitation, electron from O 2p orbitals are excited into O_h Fe 3d states. This changes the electrostatic attraction between photo-reduced Fe and the nearby O ligands, causing the Fe−O bond length to increase. This distortion of the lattice generates phonons which couple to the excited free carriers to form electron polarons as the electron becomes localized and trapped at the Fe metal centers, while the hole density is initially distributed among the bonded O ligands. Expansion of the Fe−O bond correlates with contraction of the Ni−O bond within an O_h subunit. Consequently, as holes from the O 2p valence band states thermalize to Ni 3d states at the valence band maximum, they experience increased crystal field splitting leading to the formation of a LS O_h Ni^{3+} state. A schematic of this process showing photoinduced charge transfer, electron and hole polaron formation, and spin-state transition is shown in Figure 8. While we cannot directly determine the rate of spin crossover, we can safely conclude that this rate is significantly faster than the measured time constant for hole polaron formation (0.326 ± 0.14 ps) as we never observe a transient spectrum of a HS Ni^{3+} intermediate.

CONCLUSION

We present here an investigation of the charge and spin dynamics in NFO thin films after photoexcitation using XUV-RA measurements, which provides element specific resolution of oxidation state, spin state, and coordination geometry during ultrafast optical switching. These NFO films possess a mixed spinel phase, which allows 12 possible charge transfer excitation pathways upon photoexcitation with 400 nm light. To determine the actual nature of the photoexcited state, we compare ligand-field multiplet simulations to experimental XUV spectra and determine that these films relax into a MMCT state whereby O_h Fe sites are reduced and O_h Ni sites are oxidized. Considering the possible spin configurations for photoexcited O_h Fe^{2+} and O_h Ni^{3+} shows that a spin-state transition forms a LS O_h Ni^{3+} state. Kinetic analysis reveals that this transition proceeds through a O_h Fe^{2+} LMCT intermediate, followed by fast electron and hole polaron formation, where the hole thermalizes from O 2p to Ni 3d valence band states. A spin crossover event leads to a LS O_h Ni^{3+} final state within 0.326 ± 0.14 ps. This study not only provides important mechanistic insights into the fundamental processes that mediate ultrafast optical spin switching, but also highlights the capability of XUV spectroscopy to elucidate these dynamics in complex magnetic materials with unprecedented site-specific resolution revealing the real-time evolution of charge and spin states on individual atoms.

ASSOCIATED CONTENT

Supporting Information

The Supporting Information is available free of charge at https://pubs.acs.org/doi/10.1021/acs.jpcc.1c09763.

Sample preparation, XPS sample characterization, description of the XUV spectrometer layout, explanation of the ligand field multiplet simulations, and kinetic equations (PDF)

AUTHOR INFORMATION

Corresponding Author

L. Robert Baker − *Department of Chemistry and Biochemistry, The Ohio State University, Columbus, Ohio 43210, United States;* orcid.org/0000-0001-6740-864X; Email: baker.2364@osu.edu

Authors

Stephen Londo − *Department of Chemistry and Biochemistry, The Ohio State University, Columbus, Ohio 43210, United States;* orcid.org/0000-0002-6456-9680

Somnath Biswas − *Department of Chemistry and Biochemistry, The Ohio State University, Columbus, Ohio 43210, United States;* orcid.org/0000-0002-5931-4966

Igor V. Pinchuk − *Department of Physics, The Ohio State University, Columbus, Ohio 43210, United States*

Alexandra Boyadzhiev − *Department of Physics, The Ohio State University, Columbus, Ohio 43210, United States*

Roland K. Kawakami − *Department of Physics, The Ohio State University, Columbus, Ohio 43210, United States;* orcid.org/0000-0003-0245-9192

Complete contact information is available at: https://pubs.acs.org/10.1021/acs.jpcc.1c09763

Notes

The authors declare no competing financial interest.

https://doi.org/10.1021/acs.jpcc.1c09763
J. Phys. Chem. C 2022, 126, 2669−2678

■ ACKNOWLEDGMENTS

XUV measurements, spectral simulations, and sample growth and preparation were supported by the Center for Emergent Materials, an NSF MRSEC, under Award DMR-2011876. We also thank Katie Robinson for assistance with RHEED measurements.

■ REFERENCES

(1) Tudosa, I.; Stamm, C.; Kashuba, A.; King, F.; Siegmann, H.; Stöhr, J.; Ju, G.; Lu, B.; Weller, D. The ultimate speed of magnetic switching in granular recording media. *Nature* **2004**, *428*, 831−833.
(2) Beaurepaire, E.; Merle, J.-C.; Daunois, A.; Bigot, J.-Y. Ultrafast spin dynamics in ferromagnetic nickel. *Phys. Rev. Lett.* **1996**, *76*, 4250.
(3) Hohlfeld, J.; Matthias, E.; Knorren, R.; Bennemann, K. Nonequilibrium magnetization dynamics of nickel. *Phys. Rev. Lett.* **1997**, *78*, 4861.
(4) Kimel, A.; Kirilyuk, A.; Usachev, P.; Pisarev, R.; Balbashov, A.; Rasing, T. Ultrafast non-thermal control of magnetization by instantaneous photomagnetic pulses. *Nature* **2005**, *435*, 655−657.
(5) Wang, J.; Cotoros, I.; Dani, K.; Liu, X.; Furdyna, J.; Chemla, D. Ultrafast enhancement of ferromagnetism via photoexcited holes in GaMnAs. *Phys. Rev. Lett.* **2007**, *98*, 217401.
(6) Stanciu, C.; Hansteen, F.; Kimel, A.; Kirilyuk, A.; Tsukamoto, A.; Itoh, A.; Rasing, T. All-optical magnetic recording with circularly polarized light. *Phys. Rev. Lett.* **2007**, *99*, 047601.
(7) Mangin, S.; Gottwald, M.; Lambert, C.; Steil, D.; Uhlíř, V.; Pang, L.; Hehn, M.; Alebrand, S.; Cinchetti, M.; Malinowski, G.; et al. Engineered materials for all-optical helicity-dependent magnetic switching. *Nat. Mater.* **2014**, *13*, 286−292.
(8) Schubert, C.; Hassdenteufel, A.; Matthes, P.; Schmidt, J.; Helm, M.; Bratschitsch, R.; Albrecht, M. All-optical helicity dependent magnetic switching in an artificial zero moment magnet. *Appl. Phys. Lett.* **2014**, *104*, 082406.
(9) Vomir, M.; Albrecht, M.; Bigot, J.-Y. Single shot all optical switching of intrinsic micron size magnetic domains of a Pt/Co/Pt ferromagnetic stack. *Appl. Phys. Lett.* **2017**, *111*, 242404.
(10) Gorchon, J.; Lambert, C.-H.; Yang, Y.; Pattabi, A.; Wilson, R. B.; Salahuddin, S.; Bokor, J. Single shot ultrafast all optical magnetization switching of ferromagnetic Co/Pt multilayers. *Appl. Phys. Lett.* **2017**, *111*, 042401.
(11) Villeneuve, A.; Yang, C.; Wigley, P.; Stegeman, G.; Aitchison, J.; Ironside, C. Ultrafast all-optical switching in semiconductor nonlinear directional couplers at half the band gap. *Appl. Phys. Lett.* **1992**, *61*, 147−149.
(12) Kojima, E.; Shimano, R.; Hashimoto, Y.; Katsumoto, S.; Iye, Y.; Kuwata-Gonokami, M. Observation of the spin-charge thermal isolation of ferromagnetic Ga 0.94 Mn 0.06 As by time-resolved magneto-optical measurements. *Phys. Rev. B* **2003**, *68*, 193203.
(13) Piccione, B.; Cho, C.-H.; Van Vugt, L. K.; Agarwal, R. All-optical active switching in individual semiconductor nanowires. *Nat. Nano.* **2012**, *7*, 640−645.
(14) Duong, N. P.; Satoh, T.; Fiebig, M. Ultrafast manipulation of antiferromagnetism of NiO. *Phys. Rev. Lett.* **2004**, *93*, 117402.
(15) Kalashnikova, A.; Kimel, A.; Pisarev, R.; Gridnev, V.; Usachev, P.; Kirilyuk, A.; Rasing, T. Impulsive excitation of coherent magnons and phonons by subpicosecond laser pulses in the weak ferromagnet FeBO 3. *Phys. Rev. B* **2008**, *78*, 104301.
(16) Stupakiewicz, A.; Maziewski, A.; Davidenko, I.; Zablotskii, V. Light-induced magnetic anisotropy in Co-doped garnet films. *Phys. Rev. B* **2001**, *64*, 064405.
(17) Hansteen, F.; Kimel, A.; Kirilyuk, A.; Rasing, T. Femtosecond photomagnetic switching of spins in ferrimagnetic garnet films. *Phys. Rev. Lett.* **2005**, *95*, 047402.
(18) Hansteen, F.; Kimel, A.; Kirilyuk, A.; Rasing, T. Nonthermal ultrafast optical control of the magnetization in garnet films. *Phys. Rev. B* **2006**, *73*, 014421.
(19) Atoneche, F.; Kalashnikova, A.; Kimel, A.; Stupakiewicz, A.; Maziewski, A.; Kirilyuk, A.; Rasing, T. Large ultrafast photoinduced magnetic anisotropy in a cobalt-substituted yttrium iron garnet. *Phys. Rev. B* **2010**, *81*, 214440.
(20) Suárez, C.; Bron, W.; Juhasz, T. Dynamics and transport of electronic carriers in thin gold films. *Phys. Rev. Lett.* **1995**, *75*, 4536.
(21) Fann, W.; Storz, R.; Tom, H.; Bokor, J. Electron thermalization in gold. *Phys. Rev. B* **1992**, *46*, 13592.
(22) Siegrist, F.; Gessner, J. A.; Ossiander, M.; Denker, C.; Chang, Y.-P.; Schröder, M. C.; Guggenmos, A.; Cui, Y.; Walowski, J.; Martens, U.; et al. Light-wave dynamic control of magnetism. *Nature* **2019**, *571*, 240−244.
(23) Schoenlein, R.; Lin, W.; Fujimoto, J.; Eesley, G. Femtosecond studies of nonequilibrium electronic processes in metals. *Phys. Rev. Lett.* **1987**, *58*, 1680.
(24) Ono, S. Thermalization in simple metals: Role of electron-phonon and phonon-phonon scattering. *Phys. Rev. B* **2018**, *97*, 054310.
(25) Kirilyuk, A.; Kimel, A. V.; Rasing, T. Ultrafast optical manipulation of magnetic order. *RMP* **2010**, *82*, 2731.
(26) Carneiro, L. M.; Cushing, S. K.; Liu, C.; Su, Y.; Yang, P.; Alivisatos, A. P.; Leone, S. R. Excitation-wavelength-dependent small polaron trapping of photoexcited carriers in α-Fe 2 O 3. *Nat. Mater.* **2017**, *16*, 819.
(27) Husek, J.; Cirri, A.; Biswas, S.; Baker, L. R. Surface electron dynamics in hematite (α-Fe 2 O 3): correlation between ultrafast surface electron trapping and small polaron formation. *Chem. Sci.* **2017**, *8*, 8170−8178.
(28) Bandaranayake, S.; Hruska, E.; Londo, S.; Biswas, S.; Baker, L. R. Small Polarons and Surface Defects in Metal Oxide Photocatalysts Studied Using XUV Reflection−Absorption Spectroscopy. *J. Phys. Chem. C* **2020**, *124*, 22853−22870.
(29) Lüders, U.; Barthelemy, A.; Bibes, M.; Bouzehouane, K.; Fusil, S.; Jacquet, E.; Contour, J.-P.; Bobo, J.-F.; Fontcuberta, J.; Fert, A. NiFe2O4: a versatile spinel material brings new opportunities for spintronics. *Adv. Mater.* **2006**, *18*, 1733−1736.
(30) Matzen, S.; Moussy, J.-B.; Wei, P.; Gatel, C.; Cezar, J.; Arrio, M.; Sainctavit, P.; Moodera, J. Structure, magnetic ordering, and spin filtering efficiency of NiFe2O4 (111) ultrathin films. *Appl. Phys. Lett.* **2014**, *104*, 182404.
(31) Harris, V. G. Modern microwave ferrites. *IEEE Trans. Magn.* **2012**, *48*, 1075−1104.
(32) De Groot, F.; Kotani, A. *Core Level Spectroscopy of Solids*; CRC Press: 2008.
(33) Schultze, M.; Ramasesha, K.; Pemmaraju, C.; Sato, S.; Whitmore, D.; Gandman, A.; Prell, J. S.; Borja, L.; Prendergast, D.; Yabana, K.; et al. Attosecond band-gap dynamics in silicon. *Science* **2014**, *346*, 1348−1352.
(34) Zhang, K.; Lin, M.-F.; Ryland, E. S.; Verkamp, M. A.; Benke, K.; De Groot, F. M.; Girolami, G. S.; Vura-Weis, J. Shrinking the synchrotron: Tabletop extreme ultraviolet absorption of transition-metal complexes. *J. Phys. Chem. Lett.* **2016**, *7*, 3383−3387.
(35) Zurch, M.; Chang, H.-T.; Borja, L. J.; Kraus, P. M.; Cushing, S. K.; Gandman, A.; Kaplan, C. J.; Oh, M. H.; Prell, J. S.; Prendergast, D.; Pemmaraju, C. D.; Neumark, D. M.; Leone, S. R. Direct and simultaneous observation of ultrafast electron and hole dynamics in germanium. *Nat. Commun.* **2017**, *8*, 1−11.
(36) Hofherr, M.; Moretti, S.; Shim, J.; Häuser, S.; Safonova, N. Y.; Stiehl, M.; Ali, A.; Sakshath, S.; Kim, J.; Kim, D.; et al. Induced versus intrinsic magnetic moments in ultrafast magnetization dynamics. *Phys. Rev. B* **2018**, *98*, 174419.
(37) Zürch, M.; Chang, H.-T.; Kraus, P. M.; Cushing, S. K.; Borja, L. J.; Gandman, A.; Kaplan, C. J.; Oh, M. H.; Prell, J. S.; Prendergast, D.; et al. Ultrafast carrier thermalization and trapping in silicon-germanium alloy probed by extreme ultraviolet transient absorption spectroscopy. *Struct. Dyn.* **2017**, *4*, 044029.
(38) Cirri, A.; Husek, J.; Biswas, S.; Baker, L. R. Achieving surface sensitivity in ultrafast XUV spectroscopy: M2, 3-edge reflection-absorption of transition metal oxides. *J. Phys. Chem. C* **2017**, *121*, 15861−15869.

https://doi.org/10.1021/acs.jpcc.1c09763
J. Phys. Chem. C 2022, 126, 2669−2678

(39) Liu, H.; Klein, I. M.; Michelsen, J. M.; Cushing, S. K. Element-specific electronic and structural dynamics using transient XUV and soft X-ray spectroscopy. *Chem.* **2021**, *7*, 2569−2584.
(40) Mathias, S.; Chan, L.-O.; Grychtol, P.; Granitzka, P.; Turgut, E.; Shaw, J. M.; Adam, R.; Nembach, H. T.; Siemens, M. E.; Eich, S.; et al. Probing the timescale of the exchange interaction in a ferromagnetic alloy. *Proc. Natl. Acad. Sci. U. S. A.* **2012**, *109*, 4792−4797.
(41) La-O-Vorakiat, C.; Turgut, E.; Teale, C. A.; Kapteyn, H. C.; Murnane, M. M.; Mathias, S.; Aeschlimann, M.; Schneider, C. M.; Shaw, J. M.; Nembach, H. T.; Silva, T. J. Ultrafast demagnetization measurements using extreme ultraviolet light: Comparison of electronic and magnetic contributions. *Phys. Rev. X* **2012**, *2*, 011005.
(42) Gang, S.-g.; Adam, R.; Plötzing, M.; von Witzleben, M.; Weier, C.; Parlak, U.; Bürgler, D. E.; Schneider, C. M.; Rusz, J.; Maldonado, P.; et al. Element-selective investigation of femtosecond spin dynamics in nipd magnetic alloys using extreme ultraviolet radiation. *Phys. Rev. B* **2018**, *97*, 064412.
(43) Biswas, S.; Husek, J.; Baker, L. R. Elucidating ultrafast electron dynamics at surfaces using extreme ultraviolet (XUV) reflection−absorption spectroscopy. *Chem. Commun.* **2018**, *54*, 4216−4230.
(44) Stavitski, E.; De Groot, F. M. The CTM4XAS program for EELS and XAS spectral shape analysis of transition metal L edges. *Micron* **2010**, *41*, 687−694.
(45) Londo, S.; Biswas, S.; Husek, J.; Pinchuk, I. V.; Newburger, M. J.; Boyadzhiev, A.; Trout, A. H.; McComb, D. W.; Kawakami, R.; Baker, L. R. Ultrafast Spin Crossover in a Room-Temperature Ferrimagnet: Element-Specific Spin Dynamics in Photoexcited Cobalt Ferrite. *J. Phys. Chem. C* **2020**, *124*, 11368−11375.
(46) Biswas, S.; Husek, J.; Londo, S.; Baker, L. R. Ultrafast electron trapping and defect-mediated recombination in NiO probed by femtosecond extreme ultraviolet reflection−absorption spectroscopy. *J. Phys. Chem. Lett.* **2018**, *9*, 5047−5054.
(47) Biswas, S.; Wallentine, S.; Bandaranayake, S.; Baker, L. R. Controlling polaron formation at hematite surfaces by molecular functionalization probed by XUV reflection-absorption spectroscopy. *J. Chem. Phys.* **2019**, *151*, 104701.
(48) Biswas, S.; Husek, J.; Londo, S.; Baker, L. R. Highly localized charge transfer excitons in metal oxide semiconductors. *Nano Lett.* **2018**, *18*, 1228−1233.
(49) Hoang, K. Polaron formation, native defects, and electronic conduction in metal tungstates. *Phys. Rev. Mater.* **2017**, *1*, 024603.
(50) Hoang, K.; Oh, M.; Choi, Y. Electronic structure, polaron formation, and functional properties in transition-metal tungstates. *RSC Adv.* **2018**, *8*, 4191−4196.
(51) Dileep, K.; Loukya, B.; Pachauri, N.; Gupta, A.; Datta, R. Probing optical band gaps at the nanoscale in NiFe2O4 and CoFe2O4 epitaxial films by high resolution electron energy loss spectroscopy. *J. Appl. Phys.* **2014**, *116*, 103505.

https://doi.org/10.1021/acs.jpcc.1c09763
J. Phys. Chem. C 2022, 126, 2669−2678